Chemical Science

ROYAL SOCIETY OF CHEMISTRY

EDGE ARTICLE

View Article Online
View Journal | View Issue

Check for updates

Cite this: *Chem. Sci.*, 2025, **16**, 4057

All publication charges for this article have been paid for by the Royal Society of Chemistry

Received 13th December 2024
Accepted 21st January 2025

DOI: 10.1039/d4sc08434a

rsc.li/chemical-science

Open Access Article. Published on 04 1403. Downloaded on 28/11/1404 10:53:11 ..
This article is licensed under a Creative Commons Attribution-NonCommercial 3.0 Unported Licence.

Chiral perovskites with a unique 1D chain structure: impact of chiral ligand geometry on local inversion asymmetry and chiral-induced spin selectivity†

Hongxu Li,[a] Rui Cao,[b] Min Tao,[a] Jiawei Jiang*[c] and Yin Xiao *[a]

Chiral hybrid organic–inorganic perovskites (HOIPs) have demonstrated significant potential in spintronics, primarily due to inversion symmetry breaking as well as strong spin–orbit coupling (SOC) arising from their heavy-element composition. Numerous studies have confirmed that chiral perovskites exhibit superior chiral-induced spin selectivity (CISS). However, the key factors underlying such pronounced spin polarization selectivity, especially within organic–inorganic hybrid systems, are not well understood. This oversight marks a critical area for deeper exploration in spintronics research. We introduce *R*/*S*-1-amino-2-propanol (*R*/*S*-HP1A) as a chiral spacer to synthesize chiral perovskites, (*R*/*S*-HP1A)PbI_3, characterized by a distinct 1D chain structure with two layers of inorganic octahedrons in each chain. In (*R*/*S*-HP1A)PbI_3, the chiral carbon locates away from the perovskite's inorganic skeleton, resulting in a slight degree of inversion asymmetry within the inorganic sublattice while maintaining a global chiral space group ($P2_12_12_1$). As a result, (*R*/*S*-HP1A)PbI_3 exhibits small Rashba–Dresselhaus spin-splitting, a purely in-plane spin texture, a short spin lifetime (4 ± 1.5 ps) and a relatively low polarization degree of the CISS effect (58% and 66% for *R*- and *S*-forms, respectively), in comparison to other reported low-dimensional chiral perovskites. These findings emphasize that the local inversion asymmetry of the inorganic octahedrons, beyond global chirality, significantly influences the CISS effect in chiral perovskites, which is important for targeted improvements in spintronic applications.

Introduction

Hybrid organic–inorganic perovskites (HOIPs) have emerged as highly versatile materials in various electronic and optoelectronic applications, including solar cells,[1,2] lasers,[3] light-emitting diodes,[4,5] and photodetectors.[6,7] By introducing a chiral organic intercalating spacer, chirality can be introduced into the perovskite's inorganic sublattices, endowing them with unique properties derived from their non-centrosymmetric structures, such as circular dichroism (CD) and circularly polarized light (CPL),[8,9] nonlinear optical behavior,[10,11] ferroelectricity,[12] *etc.* Crucially, the inorganic framework of HOIPs, composed of heavy elements such as lead and halide, exhibits significant spin–orbit coupling (SOC).[13] This characteristic greatly enhances their potential for spintronics applications, presenting exciting opportunities for the development of advanced electronic devices.

Among various chirality-related physics, chiral-induced spin selectivity (CISS) stands out as particularly significant. Since the pioneering study of CISS in 1999,[14] extensive experimental and theoretical research has explored the underlying physics and mechanisms of this intriguing effect. CISS refers to the ability of chiral materials to function as spin filters during electron transport. As electrons traverse a chiral structure, their spin states are selectively aligned with the material's intrinsic chirality. This phenomenon enables the generation of spin-polarized electrons without relying on external magnetic fields or ferromagnetic materials, offering significant potential for advanced spintronic applications. In recent years, a plethora of studies have prepared various 2D and 1D chiral perovskites and assessed their CISS effects using magnetic conductive probe atomic force microscopy (mCP-AFM).[15–18] These studies reveal that most chiral perovskite structures demonstrate a spin polarization selectivity of up to over 80%, significantly surpassing those of chiral organic molecules, which range from 30 to 50%. Despite these findings, the origins of such high spin polarization selectivity in chiral perovskites, particularly as an organic–inorganic hybrid system, have received relatively little attention. This gap highlights a crucial area for further investigation within the field of spintronics.

[a]*School of Chemical Engineering and Technology, Tianjin University, Tianjin 300350, China. E-mail: xiaoyin@tiu.edu.cn*

[b]*School of Science, Tianjin University, Tianjin 300350, China*

[c]*National Laboratory of Solid-State Microstructures, School of Physics, Collaborative Innovation Center of Advanced Microstructures, Nanjing University, Nanjing 210093, China. E-mail: jiangjiawei@nju.edu.cn*

† Electronic supplementary information (ESI) available. CCDC 2372496 and 2372497. For ESI and crystallographic data in CIF or other electronic format see DOI: https://doi.org/10.1039/d4sc08434a

© 2025 The Author(s). Published by the Royal Society of Chemistry

Open Access Article. Published on 04 1403. Downloaded on 28/11/1404 10:53:11 ..
This article is licensed under a Creative Commons Attribution-NonCommercial 3.0 Unported Licence.

In 2019, Beard[15] *et al.* first demonstrated the CISS effect in 2D chiral perovskites (*R*/*S*-MBA_2PbI_4) using chiral methylphenethylamine (*R*/*S*-MBA) as the intercalating spacer, achieving an impressive spin polarization degree of 86%. Subsequently, they reported an even higher spin polarization selectivity of 93–94% in their 2D Sn-based analogues (*R*/*S*-MBA_2SnI_4).[16] This remarkable selectivity was attributed to the cumulative CISS effect as carriers traversed multiple chiral organic layers within the organic–inorganic 2D layered perovskites. In parallel, Song[17] *et al.* observed that 1D chiral perovskites (*R*/*S*-$MBAPbBr_3$) also exhibited high spin polarization efficiency, reaching up to 90%. Unlike the corner-sharing arrangement typical in 2D layered chiral structures, the inorganic octahedra in these 1D chiral perovskites are linked in a plane-sharing manner. However, both 1D and 2D configurations exhibit comparably high spin polarization selectivity. This led to the conclusion that the primary determinant of spin selectivity in HOIPs is the global structural chirality induced by chiral molecules, and inorganic factors such as the electronic structure (*i.e.*, band gap) and the crystal structure (*i.e.*, PbX_6^{4-} octahedral framework) appear to have minimal impact.[15–17] However, the theoretical description of CISS must account for SOC, which is essential for coupling electron motion and spin.[14,19] It is the SOC within the chiral system that causes the change in the spin energy of the moving electrons.[20] In HOIPs, strong SOC primarily arises from the inorganic skeleton, which is composed of heavy atoms, suggesting that the inorganic octahedral skeleton and its inversion asymmetry could also play a crucial role in the CISS effect. This underscores the importance of research into the influence of the inorganic structure on the spin-related and CISS properties of chiral perovskites.

Herein, we selected 1-amino-2-propanol (*R*/*S*-HP1A) (Scheme 1) as a chiral intercalating spacer to synthesize chiral perovskite single crystals (*R*/*S*-HP1A)PbI_3 with a chiral space group of $P2_12_12_1$. These crystals feature a 1D chain structure where each chain comprises two line-sharing octahedron layers. Two inorganic octahedrons on adjacent 1D chains are directly connected by the same organic chiral molecule, resulting in relatively weak confinement and localization of the electronic states derived from the inorganic components. Unlike typical chiral intercalating spacers such as *R*/*S*-MBA, used in most reported 1D and 2D chiral perovskites, the chiral carbon in *R*/*S*-HP1A is not directly linked to the amino group. This configuration places the chiral carbon relatively far from the inorganic octahedron. Consequently, despite the global chiral space group, a small degree of local chirality in the inorganic octahedron is generated, thus leading to small Rashba–Dresselhaus spin-splitting and a spin texture with no surviving *z* component of spin expectation $\langle\sigma_z\rangle$ and a short spin lifetime (4 ± 1.5 ps). Moreover, we observed a CISS effect with relatively low spin polarization degrees (58% and 66% for *R*- and *S*-forms, respectively), suggesting that factors beyond chiral organic molecules and the global chiral space group, like the local chirality of the inorganic layer and the extent of spin-splitting it controls, significantly influence CISS. Our findings introduce the previously overlooked aspect of local chirality in the inorganic skeleton, offering new insights for understanding the high spin polarization selectivity observed in chiral HOIPs.

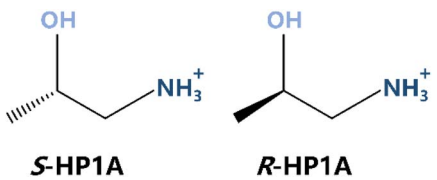

Scheme 1 Structures of the chiral cations.

Results and discussion

Crystal structure of chiral (*R*/*S*-HP1A)PbI_3

Chiral (*R*/*S*-HP1A)PbI_3 single crystals are synthesized using methyl acetate as an antisolvent in a hydroiodic acid solution. Crystallographic data and structural refinement information are provided in Table S1,† with images of the (*R*-HP1A)PbI_3 crystals (Fig. S1†). The single crystal X-ray structures are solved in a $P2_12_12_1$ chiral space group, which is similar to most reported 1D chiral perovskites.[17,21–23] Each cell unit contains four PbI_6^{4-} inorganic units and four HP1A (Fig. S2†). Different from typical chiral 1D perovskites, where face-sharing PbI_6^{4-} octahedral chains are surrounded by organic chiral cations,[17,21–25] (*R*/*S*-HP1A)PbI_3 features a 1D chain structure with two layers of line-sharing octahedrons in each chain. Along the *c*-axis, one I atom in the axial direction and one I atom in the equatorial plane of an octahedron in the upper layer occupy respectively an equatorial plane and axial position of the octahedron in the lower layer, designated as I_1. Iodine atoms shared by two adjacent octahedra only along the *a*-axis are denoted as I_2, while the axial iodine atoms not involved in octahedral sharing are labeled as I_3. Fig. 1a and b illustrate how two PbI_6^{4-} octahedrons are connected by line-sharing four iodine atoms (I_2–I_1–I_1–I_2), with these linked octahedrons further extending into a 1D chain along the *a*-axis through line-sharing of two iodine atoms (I_1–I_2). To assess the deviation of the inorganic octahedral framework in (*R*/*S*-HP1A)PbI_3, we calculated the octahedral secondary elongation (λ_{oct}) and bond angle variance (σ_{oct}^2) as defined by Robinson *et al.*, which can be quantified using the following equations:[26]

$$\lambda_{oct} = \frac{1}{6}\sum_{n=1}^{6}\left(\frac{d_n - d_{avg}}{d_{avg}}\right)^2 \quad (1)$$

$$\sigma_{oct}{}^2 = \frac{1}{11}\sum_{n=1}^{12}(\theta_n - 90^\circ)^2 \quad (2)$$

where d_n represents the length of each Pb–I bond, d_{avg} is the average length of all Pb–I bonds, and θ_n is the angle formed by each I–Pb–I bond. As shown in Table S2,† the calculated λ_{oct} and $\sigma_{oct}{}^2$ for both (*R*-HP1A)PbI_3 and (*S*-HP1A)PbI_3 are similar. The line-sharing PbI_6^{4-} octahedrons in the upper and lower layers present identical λ_{oct} and $\sigma_{oct}{}^2$ values (Tables S3 and S4†). Along with these results, we also computed the structural parameters for other known Pb-based helical 1D chiral perovskites and

© 2025 The Author(s). Published by the Royal Society of Chemistry

Open Access Article. Published on 04 1403. Downloaded on 28/11/1404 10:53:11 ..
This article is licensed under a Creative Commons Attribution-NonCommercial 3.0 Unported Licence.

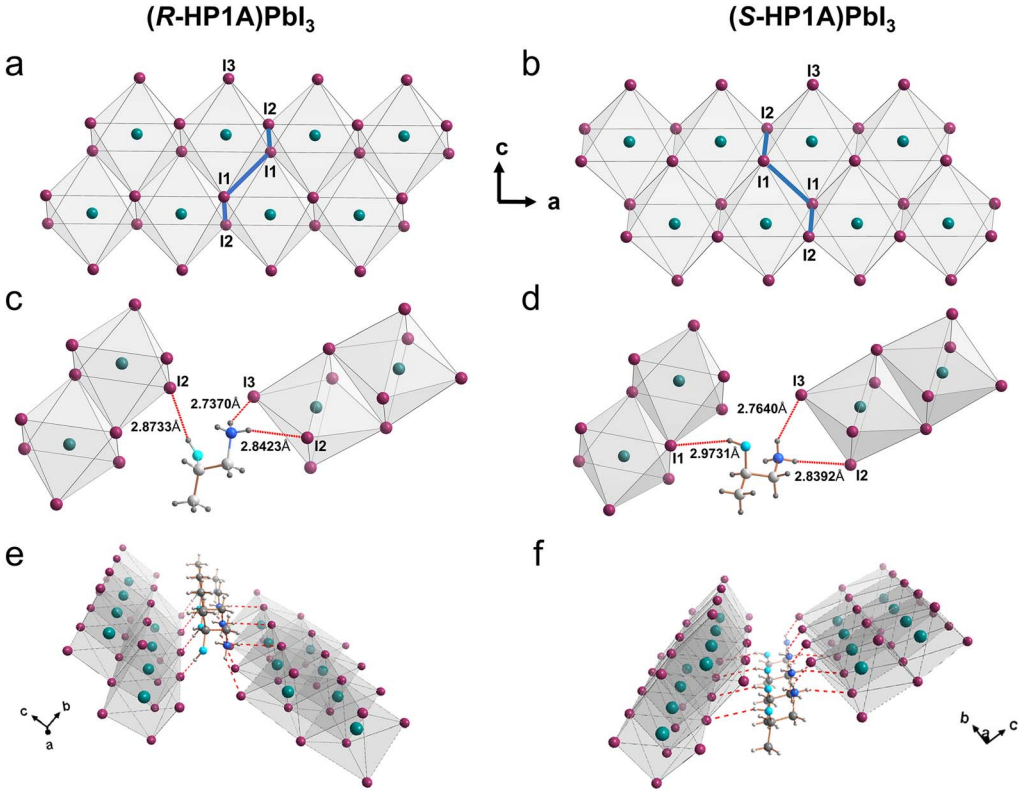

Fig. 1 (a and b) Structures of (a) (*R*-HP1A)PbI_3 and (b) (*S*-HP1A)PbI_3. (c and d) The hydrogen bonds between the organic cations and inorganic octahedra in (c) (*R*-HP1A)PbI_3 and (d) (*S*-HP1A)PbI_3. (e and f) The adjacent inorganic octahedral chains in (e) (*R*-HP1A)PbI_3 and (f) (*S*-HP1A)PbI_3 connected by hydrogen bonding *via* the HP1A molecule (the red lines represent the intramolecular hydrogen bonding).

their 2D analogues, which are compiled in Table S5.† As a general trend, helical 1D chiral perovskites exhibit larger λ_{oct} and σ_{oct}^2 values compared to chiral 2D structures. This difference arises because the face-sharing 1D structure necessarily has a larger distortion than the corner-sharing 2D inorganic skeleton. For (*R*/*S*-HP1A)PbI_3, the inorganic skeletons present a line-sharing feature, which reduces the number of I atoms shared between adjacent octahedrons and allows for increased structural flexibility compared to other face-sharing 1D chiral perovskites, resulting in a relatively smaller σ_{oct}^2 close to that of the 2D structure. However, (*R*/*S*-HP1A)PbI_3 presents larger λ_{oct} than most reported chiral 1D and 2D structures. The lengths of each Pb–I bond in the two layers of line-sharing octahedra are detailed in Table S3.† In (*R*/*S*-HP1A)PbI_3, the iodine atoms shared by the upper and lower layer octahedra are positioned in the equatorial plane of one octahedron and in the axial direction of the other. This unique arrangement must lead to significant stretching of the bond length between I_1 and Pb (Fig. S3†). Strong hydrogen bonding interactions are observed between iodine atoms in the inorganic octahedrons and the hydrogen atoms from the amino and hydroxy groups of the organic spacer. Specifically, two hydrogen atoms on the amino group of *R*/*S*-HP1A are connected with I_2 and I_3 of the inorganic octahedrons (*R*: N–H···I_2-2.8423 Å, N–H···I_3-2.7370 Å, *S*: N–H···I_2-2.8392 Å, and N–H···I_3-2.7640 Å) (Fig. 1b and c). In (*R*-HP1A)PbI_3, the hydroxyl group of HP1A forms hydrogen bonds with I_2, and in (*S*-HP1A)PbI_3, it connects with I_1. These hydrogen bonds directly connect two inorganic octahedrons in adjacent 1D chains *via* the same HP1A molecule (Fig. 1e and f), distinguishing them from typical chiral 2D and 1D structures, where adjacent PbI_6^{4-} octahedral sheets or chains are linked by van der Waals forces between two layers of chiral organic spacers. This compact connection of inorganic octahedrons leads to a relatively short distance between adjacent octahedral chains in (*R*/*S*-HP1A)PbI_3 (~7 Å, Fig S4†), which may affect the effective SOC.

Properties of chiral (*R*/*S*-HP1A)PbI_3

The CD spectra of (*R*/*S*-HP1A)PbI_3 were collected using their polycrystalline thin films, which were fabricated by spin-casting a DMF solution of the corresponding crystals. The X-ray diffraction (XRD) spectra of the (*R*/*S*-HP1A)PbI_3 thin films show sharp diffraction peaks, which is in good agreement with the simulated and single crystal powder XRD patterns (Fig. S5†), confirming the stoichiometry and crystal structure. All peaks display a narrow width, indicating a high degree of crystallinity with few impurity phases. The sharp diffraction peaks at $2\theta \approx 8.6°$, assigned to the (002) plane[23] (Fig. S5†), indicate a highly preferred orientation along the *c*-axis, which is perpendicular to the plane of the film (Fig. S6†). A mirror-image bisignate cotton effect at ~418 nm corresponding to the extinction band edge of (*R*/*S*-HP1A)PbI_3 is observed by a sharp peak corresponding to

Open Access Article. Published on 04 1403. Downloaded on 28/11/1404 10:53:11 ..
This article is licensed under a Creative Commons Attribution-NonCommercial 3.0 Unported Licence.

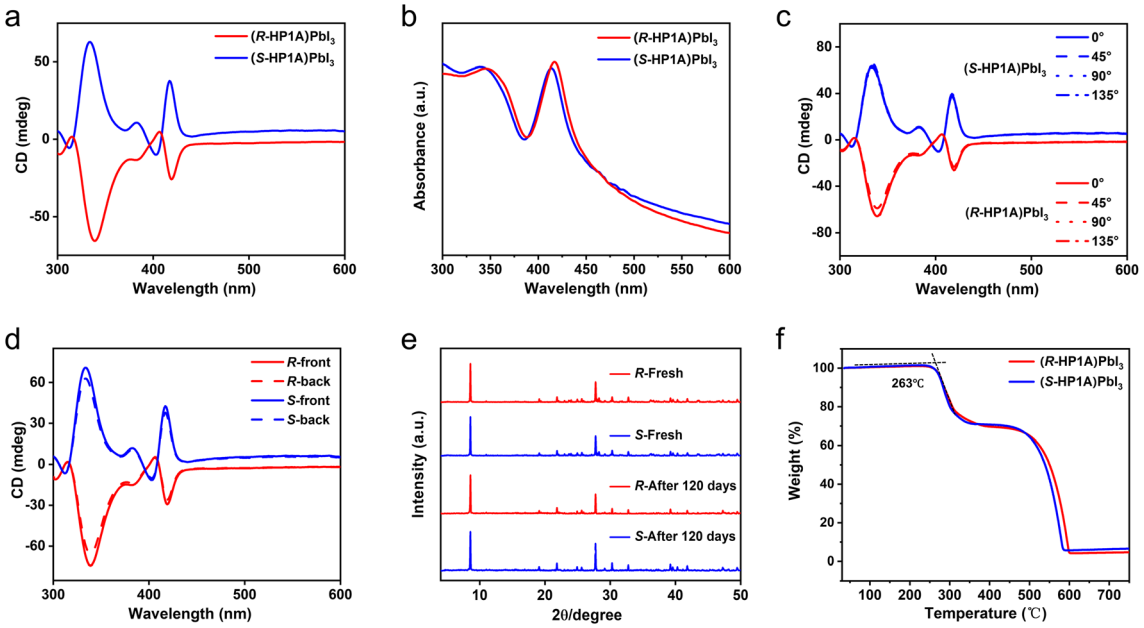

Fig. 2 (a and b) CD (a) and UV-vis absorption (b) spectra of (*R*/*S*-HP1A)PbI_3 films. (c and d) Angle-dependent (c) and direction-dependent (d) CD spectra of (*R*/*S*-HP1A)PbI_3 films. (e) XRD patterns of (*R*/*S*-HP1A)PbI_3 single crystals before and after 120 days. (f) TGA of (*R*/*S*-HP1A)PbI_3.

the first exciton transition and thus signifies the optical band gap (Fig. 2a and b). The derivative-like CD response around the band edge (405 nm and 418 nm) suggests the lifting of the spin degeneracy within the band edge electronic states.[15] The CD signals at ~340 nm relate to coupling of electric dipole transition moments between the *R*/*S*-HP1A and the inorganic part.[9] The CD spectra of (*R*/*S*-HP1A)PbI_3 display consistent patterns irrespective of sample orientation or whether measurements were taken from the front or back (Fig. 2c and d), confirming that the observed chiroptical properties indeed arise from the intrinsic chirality of (*R*/*S*-HP1A)PbI_3 and not from optical effects like linear dichroism (LD) or linear birefringence (LB). Furthermore, the air stability of the (*R*/*S*-HP1A)PbI_3 crystals was assessed using XRD, with results depicted in Fig. 2e. Even after 120 days of air exposure, the perovskite powders maintain sharp and intact diffraction peaks, demonstrating excellent resistance to oxidation. Additionally, thermal gravimetric analysis (TGA) of these chiral crystals showed that they can withstand temperatures up to ~260 °C without decomposing (Fig. 2f), highlighting their remarkable thermal stability.

Electronic structures of (*R*/*S*-HP1A)PbI_3

The electronic band structure of (*R*/*S*-HP1A)PbI_3 was calculated by density functional theory (DFT) based first-principles calculations, where the extension direction of the 1D chain points towards the *a*-axis (Fig. 3a). Accordingly, the Γ–X, Γ–Y, and Γ–Z paths in the Brillouin zone coincide, respectively, with the *a*-, *b*-, and *c*-directions of the perovskite chain in both relaxed and experimental single crystal structures (Fig. 3b). (*R*/*S*-HP1A)PbI_3 features a direct bandgap with both the CBM and VBM located at the same Γ point (Fig. 3c and d). According to the density of state (DOS) and band structure profiles (Fig. 3e, f and S7†), similar to most Pb-based 1D and 2D chiral perovskites, the CBM and VBM are mainly derived from the metal halide framework. Specifically, the VBM is mainly composed of I-p and Pb-s states, while the CBM consists mainly of Pb-p and I-s states (Fig. S8 and S9†). Different from the near-flat *E*–*k* dispersion in many 1D structures and typical 2D-like dispersion in chiral 2D perovskites, (*R*/*S*-HP1A)PbI_3 exhibits band dispersion along the Γ–X, Γ–Y, and Γ–Z paths (Fig. 3c and d). This pattern suggests that the 1D inorganic chains in (*R*/*S*-HP1A)PbI_3 are coupled in all three directions and the inorganic-derived electronic states are less confined and localized, which is likely due to the direct connection between two inorganic chains through a layer of HP1A *via* hydrogen bonding. The adjacent energy states of HP1A, Pb and I, as shown in Fig. 3e and f, suggest a weak coupling between the inorganic and organic components. Additionally, the charge density difference images (Fig. 3g and h) reveal electron accumulation and dissipation on the amino and hydroxyl surfaces of HP1A, further illustrating the correlation between organic molecules and the inorganic octahedra, which is mediated by ammonium and oxygen ions.[17]

Local asymmetry in the inorganic sublattice and Rashba–Dresselhaus spin-splitting

In 2D hybrid perovskites, the chirality of the inorganic layer plays a pivotal role in dictating spin-dependent properties. This is because in the context of the electron band structure, the front band usually originates from the inorganic component, and the SOC mainly depends on the heavy atoms that constitute the inorganic skeleton. Typically, chiral perovskites inherit their chirality from chiral organic cations, rendering the spatial relationship between the chiral carbon and the inorganic framework critical for the degree of chirality in the inorganic

© 2025 The Author(s). Published by the Royal Society of Chemistry

Open Access Article. Published on 04 1403. Downloaded on 28/11/1404 10:53:11 ..
This article is licensed under a Creative Commons Attribution-NonCommercial 3.0 Unported Licence.

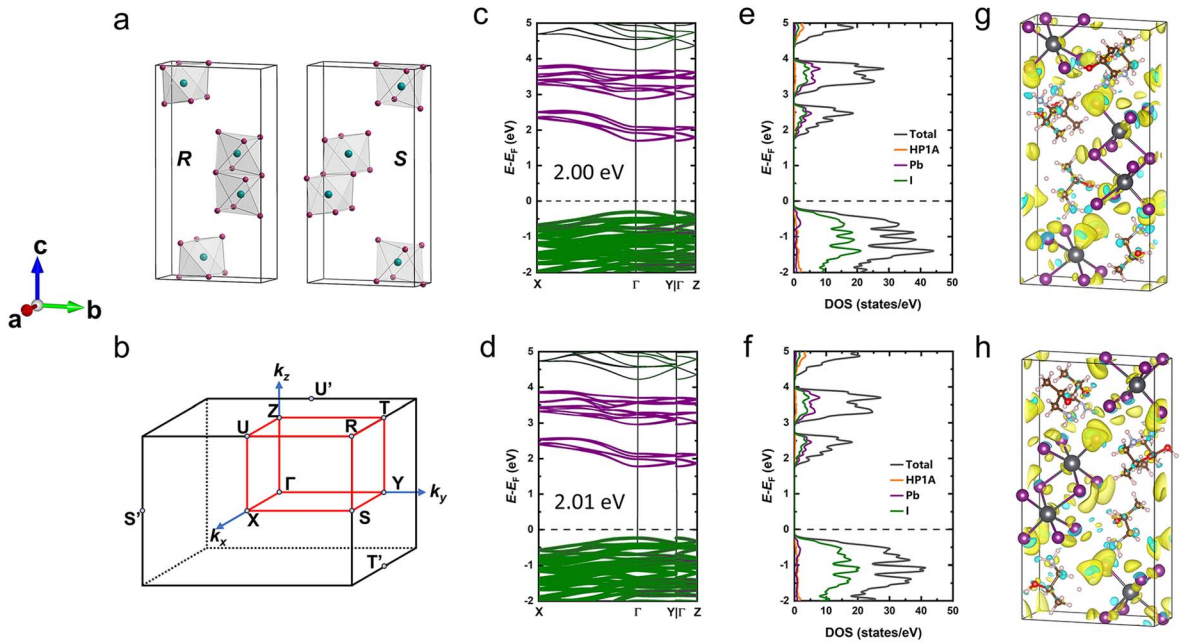

Fig. 3 (a) A representative unit cell of (*R*/*S*-HP1A)PbI_3 (organic cations are omitted). (b) Brillouin zone in the reciprocal space used for band structure calculations. (c and d) DFT-PBE + SOC band structures of (c) (*R*-HP1A)PbI_3 and (d) (*S*-HP1A)PbI_3 along the select *k*-paths. Pb-, I- and organic-derived electronic states are highlighted in purple, green and black colors, respectively. (e and f) DFT-PBE + SOC DOS of (e) (*R*-HP1A)PbI_3 and (f) (*S*-HP1A)PbI3. (g and h) Charge density differences of (g) (*R*-HP1A)PbI_3 and (h) (*S*-HP1A)PbI_3. The isosurface value is 0.0015*e* $bohr^{-3}$. The yellow and blue regions correspond to the charge accumulation and dissipation, respectively.

layer. In commonly studied 1D and 2D chiral perovskites, chiral organic cations such as *R*/*S*-MBA and *R*/*S*-NEA are utilized, where the chiral carbon is bonded to the amino group and this group typically occupies or is located near the A-site of the inorganic perovskite framework. Consequently, the chiral carbon atom is very close to the inorganic octahedron, leading to a significant degree of inversion asymmetry within the inorganic part. However, in the organic spacer structure studied (*R*/*S*-HP1A), the chiral carbon is not directly linked to the amino group (Scheme 1), a notable deviation from the typical configuration seen in the commonly used chiral organic spacers. Consequently, the spatial relationship between the chiral carbon and the inorganic octahedrons differs from those of other reported 1D or 2D single crystal structures. To quantitatively describe this relationship, we introduce a variable *X*, defined as the vertical distance from the chiral carbon of the chiral organic spacer to the plane formed by the axial iodine atoms of the octahedrons (Fig. 4a). The values of *X* for (*R*-HP1A)PbI_3, along with those for other reported 1D and 2D chiral perovskite structures, are compiled in Table S6,† providing a comparative analysis of spatial configurations across different systems. In typical chiral 2D crystal structures using *R*-MBA, the amino group occupies the A-site in the perovskite, bringing the chiral carbon connected to it in very close proximity to the inorganic framework. This configuration results in the smallest *X* value of 0.3472 Å (Fig. S10a and Table S6†). In typical 1D chiral perovskite structures (Fig. S10b, c and d†), the chiral carbon accompanied by amino group intersperses among the octahedral chains along the *b*-axis, leading to relatively small *X* values (*R*-MBAPbI_3: 0.5669 Å, *R*-NEAPbI_3: 0.5132 Å, and *R*-MPDPbI_3: 0.6898 Å). In contrast, 2D chiral perovskites (*R*-HP1A$_2$$PbBr_4$) employing the same chiral organic cations as in this work exhibit a larger *X* value (1.8374 Å) due to the chiral carbon not being directly linked to the amino group that occupies the perovskite's A-site (Fig. S10e and Table S6†). In (*R*/*S*-HP1A)PbI_3 (Fig. S4b and c†), the amino group is located further from the A site at 2.2554 Å, resulting in a significantly increased distance between the chiral carbon atom and the inorganic framework (*X* = 4.3263 Å and 4.3340 Å). While the chiral spacer cation establishes that the overall structure of the perovskite is characterized by a chiral space group, the local chirality or inversion asymmetry of the isolated inorganic chains is significantly influenced by the type and degree of specific bond angle distortions, which are closely related to the parameter *X*. The adjacent Pb atoms of (*R*/*S*-HP1A)PbI_3 within any set of four line-sharing octahedrons (labeled Pb1, Pb2, Pb3 and Pb4) in the 1D inorganic chain are coplanar (Fig. 4d), establishing a geometric center point for these octahedra and thus conferring centrosymmetry to the four Pb atoms. At the same time, we found that the Pb–I–Pb bond angles between adjacent octahedra are very close to each other, with two opposing Pb–I–Pb bonds exhibiting exactly equal angles (Fig. 4e and f). This suggests that the isolated inorganic layers are nearly centrosymmetric and possess a low local inversion asymmetry in (*R*/*S*-HP1A)PbI_3, which is likely to significantly impact their spin-related properties.

In accordance with the theoretical picture of Rashba–Dresselhaus spin-splitting, breaking of inversion symmetry in (*R*/*S*-

Open Access Article. Published on 04 1403. Downloaded on 28/11/1404 10:53:11 ..
This article is licensed under a Creative Commons Attribution-NonCommercial 3.0 Unported Licence.

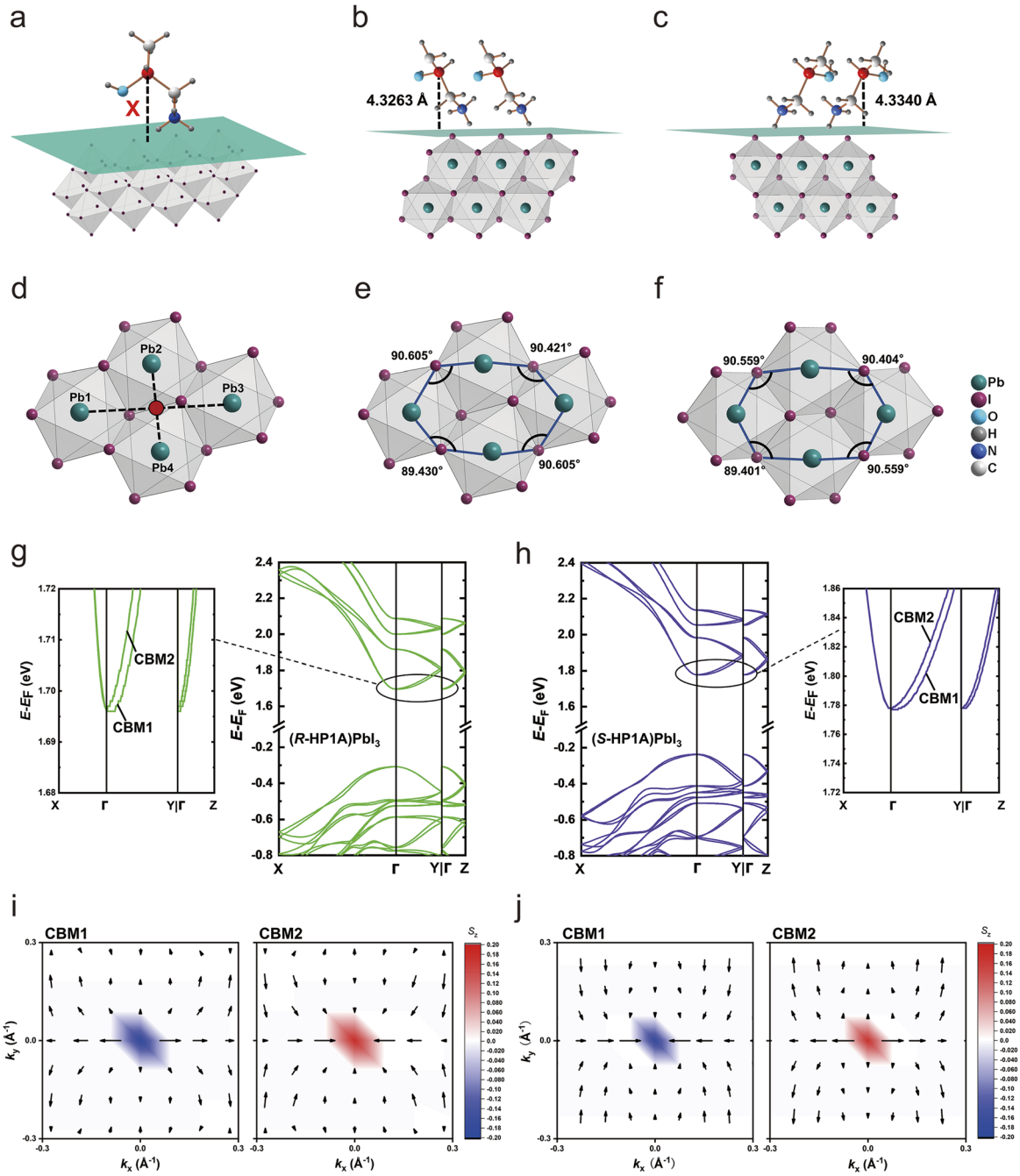

Fig. 4 (a) Schematic diagram of the vertical distance X of chiral carbon from the plane formed by the octahedral axial I atom. (b and c) The vertical distance of chiral carbon in (b) (*R*-HP1A)PbI_3 and (c) (*S*-HP1A)PbI_3 to the plane formed by the axial I atom of the octahedron. (d) Schematic diagram of four connected octahedral (set) geometric center points. (e and f) Pb–I–Pb bond angle formed between adjacent octahedrons of (e) (*R*-HP1A)PbI_3 and (f) (*S*-HP1A)PbI_3. (g and h) DFT-PBE + SOC band structures of (g) (*R*-HP1A)PbI_3 and (h) (*S*-HP1A)PbI_3 and the spin-split band edges are highlighted in the zoomed-in images. (i and j) Spin textures of conduction bands in the k_x–k_y plane for CBM1 and CBM2 of (i) (*R*-HP1A)PbI_3 and (j) (*S*-HP1A)PbI_3. The arrows indicate the in-plane spin components. The z component of spin expectation $\langle\sigma_z\rangle$ is shown by the background color.

HP1A)PbI_3 leads to the lifting of the two-fold spin degeneracy in both the conduction band (CB) and the valence band (VB), with more pronounced splitting observed in the CB (Fig. 4g and h). It can be understood from the fact that the VB states are composed principally of 5p atomic orbitals of the lighter I atoms, whereas the CB states are derived from the 6p orbitals of the heavier Pb atoms (Fig. 3c, d and S9†). Spin-splitting is observed along the Γ–Y and Γ–Z paths (Fig. 4g and h). This is because the two octahedra from adjacent inorganic chains in (*R*/*S*-HP1A)PbI_3 are directly linked *via* the same *R*/*S*-HP1A molecule, leading to weak confinement and localization of the inorganic-derived states. From the momentum shift (k_R) and

© 2025 The Author(s). Published by the Royal Society of Chemistry

Open Access Article. Published on 04 1403. Downloaded on 28/11/1404 10:53:11 ..
This article is licensed under a Creative Commons Attribution-NonCommercial 3.0 Unported Licence.

the energy splitting (ΔE), we deduced the Rashba coefficient (λ), $\lambda = \Delta E/(2k_R)$, to quantify the strength of the Rashba splitting in the CB of (R/S-HP1A)PbI_3. The resulting Rashba coefficients, $\lambda_R^{\Gamma-Y} \approx$ 59 meV Å and $\lambda_R^{\Gamma-Z} \approx$ 60 meV Å for (R-HP1A)PbI_3, $\lambda_S^{\Gamma-Y} \approx$ 72 meV Å and $\lambda_S^{\Gamma-Z} \approx$ 59 meV Å for (S-HP1A)PbI_3, are one order of magnitude lower than those of other reported low-dimensional chiral perovskites (Table S7†). This is because local distortion and consequent local asymmetry within inorganic layers must be the basis and controlling factor for spin-splitting. Consequently, although (R/S-HP1A)PbI_3 possesses a global chiral space group from the molecular organic sublattice, the spin-splitting remains weak due to the low local inversion asymmetry within the inorganic layer. The low local asymmetry within the inorganic sublattice also significantly affects the spin texture of (R/S-HP1A)PbI_3. Although the spin textures present a mixed Rashba–Dresselhaus spin-splitting, a close inspection of the spin texture reveals that the Dresselhaus spin-splitting, originating from inversion asymmetry (Fig. 4i, j and S11†), is more pronounced compared to the Rashba spin-splitting, which arises from structural inversion asymmetry. Unlike most other chiral perovskites reported, the spin texture of (R/S-HP1A)PbI_3 is almost purely in the xy-plane, with no surviving $\langle\sigma_z\rangle$ component. This suggests that the polarization field due to inversion symmetry breaking is primarily along the z direction (the direction of 1D inorganic chain stacking) and lacks a component in the xy-plane direction (the direction of 1D inorganic chain extension).[27] This is also attributable to the low local inversion asymmetry within the inorganic layer in the crystal structure, as discussed above. Moreover, (R-HP1A)PbI_3 and (S-HP1A)PbI_3 show opposite spin orientations as expected. We also investigated the spin dynamics of (R-HP1A)PbI_3 at room temperature by circularly polarized transient absorption (TA) spectroscopy. The spin relaxation dynamics are depicted in ESI,† where the spin lifetime is estimated to be 4 ± 1.5 ps (Fig. S12†), as determined from the difference between the same-circularly and counter-circularly polarized pump/probe signals ($\Delta R(\sigma^-\sigma^-) - \Delta R(\sigma^+\sigma^-)$). This spin lifetime for (R-HP1A)PbI_3 is significantly shorter compared to that of chiral perovskites reported so far (>1800 ps),[28] but is more comparable to the spin lifetime observed in achiral perovskites.[29,30] This finding indicates that the local inversion asymmetry within the inorganic sublattice has a substantial impact on the spin dynamics in perovskites.

Chiral-induced spin selectivity of (R/S-HP1A)PbI_3

The mCP-AFM measurements were performed to reveal the CISS effect in (R/S-HP1A)PbI_3 with a global chiral space group but low local inversion asymmetry in the inorganic framework. The magnetic tip is magnetized upwards or downwards relative to the substrate to inject spin-polarized current into the perovskite film fabricated by spin-casting a DMF solution of the crystals on an FTO-coated glass substrate. The thickness of the thin films is measured to be 80 ± 12 nm. The conductivity of the film in the out-of-plane direction is $(8.83 \pm 1.61) \times 10^{-9}$ S cm^{-1} for (R-HP1A)PbI_3 and $(5.91 \pm 1.12) \times 10^{-9}$ S cm^{-1} for (S-HP1A)PbI_3. The current–voltage (I–V) curves for each chiral perovskite film were averaged over 30 scans at different locations (Fig. S13†), with the shaded region around the lines representing the standard deviation for the average results. Under an electric bias voltage (−3 ∼ 3 V), the magnitude of spin current with a particular spin orientation is related to the chirality of the film. For (R-HP1A)PbI_3, spin-down current is much higher than spin-up current (Fig. 5). Conversely, (S-HP1A)PbI_3 presents opposite behavior. This indicates a preferential transfer of carriers with differing spin orientations depending on the chirality of the film, demonstrating the CISS effect in (R/S-HP1A)PbI_3. The degree of spin polarization was quantified using the formula $P = =(I_+ - I_-)/(I_+ + I_-) \times 100\%$, where I_+ and I_- represent the measured currents with the tip's magnetic field oriented upwards and downwards, respectively. The resulting spin-polarized currents reveal P values of 58% for (R-HP1A)PbI_3 and 66% for (S-HP1A)PbI_3, which are considerably lower than those typically observed in 2D and 1D chiral perovskites (generally higher than 80%). These findings suggest that the degree of spin polarization in the CISS effect of chiral perovskites may not solely be influenced by the organic chiral molecules but also by the local chirality or the degree of inversion asymmetry within the inorganic layer and the extent of spin-splitting it governs. After all, the theoretical description of the CISS effect must include SOC, and it is the SOC in chiral materials that results in changes in the energy of the spin states of the moving electrons.[20] In chiral perovskites, SOC predominantly arises from the inorganic octahedrons composed of heavy atoms; thus, a significant degree of inversion asymmetry in these isolated inorganic octahedrons may be crucial for achieving high degrees of spin polarization in CISS. In addition, the electron localization in the inorganic chains of (R/S-HP1A)PbI_3 is relatively low due to the unique connection pattern between the inorganic chains and organic molecules, as discussed above. In contrast, most reported 1D and 2D chiral perovskites with a high spin polarization degree exhibit high electron localization within the inorganic components due to

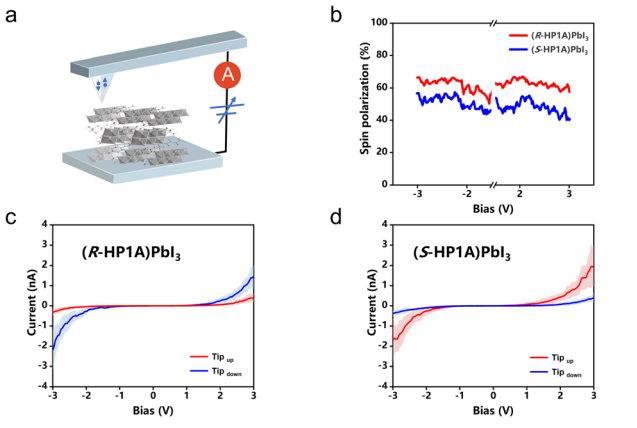

Fig. 5 (a) Schematic representation of the mCP-AFM measurements. (b) Average values of spin polarization in (R-HP1A)PbI_3 (red) and (S-HP1A)PbI_3 (blue). (c and d) Room-temperature mCP-AFM measurements for (R/S-HP1A)PbI_3. The shaded region around the lines marks the standard deviation for the average results.

Open Access Article. Published on 04 1403. Downloaded on 28/11/1404 10:53:11 ..
This article is licensed under a Creative Commons Attribution-NonCommercial 3.0 Unported Licence.

the strong confinement. The delocalized electronic states in our crystals restrict the CISS effect to a narrow energy window,[31] which may also account for the relatively low spin polarization degree observed. Notably, 2D chiral perovskites (*R*/*S*-HP1A$_2$-PbBr$_4$) utilizing *R*/*S*-HP1A with a large *X* value and a low degree of electron localization also exhibit low spin polarization (±40–45%).[14] We wish to emphasize that both the local asymmetry and the electronic state of the inorganic framework in chiral perovskites may be critical factors influencing the spin polarization degree of CISS, a consideration that has been generally overlooked in previous studies.

Conclusions

In summary, we fabricated chiral HOIPs, (*R*/*S*-HP1A)PbI$_3$, and investigated their spin-related properties. (*R*/*S*-HP1A)PbI$_3$ possesses a chiral space group of $P2_12_12_1$ and features a 1D chain structure composed of two line-sharing octahedral layers. Despite the global chiral space group, a low degree of local chirality of the inorganic octahedron is induced by the organic chiral spacer due to the large distance between the chiral carbon and the inorganic octahedron. Consequently, small Rashba–Dresselhaus spin-splitting, in-plane spin texture, a short spin lifetime (4 ± 1.5 ps) and the CISS effect with relatively low spin polarization degrees (58% and 66% for *R*- and *S*-forms, respectively) are observed. Our findings suggest that the degree of spin polarization in chiral perovskites under the CISS effect is inherently linked to its inorganic component, offering a new perspective on spin polarization selectivity principles.

Data availability

The data are available on request from the authors. Crystallographic data for 2372496 and 2372497 have been deposited at the CCDC and can be obtained from **https://www.ccdc.cam.ac.uk/**.

Author contributions

Y. X. and J. J. supervised the project. H. L. performed the single crystal and related property tests; H. L., R. C. and M. T. performed the CD, XRD and TGA tests; J. J. performed calculations. H. L. wrote the initial draft and all authors contributed to the final manuscript.

Conflicts of interest

There are no conflicts to declare.

Acknowledgements

We acknowledge Menghui Jia for help with TA measurements. We gratefully acknowledge the financial support from the National Natural Science Foundation of China (No. 22476148) and the Postdoctoral Fellowship Program of CPSF (No. GZC20240694).

References

1 K.-G. Lim, S. Ahn, Y.-H. Kim, Y. Qi and T.-W. Lee, *Energy Environ. Sci.*, 2016, **9**, 932–939.
2 S. S. Mali, J. V. Patil, J. A. Steele, M. K. Nazeeruddin, J. H. Kim and C. K. Hong, *Energy Environ. Sci.*, 2024, **17**, 1046–1060.
3 Y. Jia, R. A. Kerner, A. J. Grede, B. P. Rand and N. C. Giebink, *Nat. Photonics*, 2017, **11**, 784–788.
4 K. Wang, L. Jin, Y. Gao, A. Liang, B. P. Finkenauer, W. Zhao, Z. Wei, C. Zhu, T. F. Guo, L. Huang and L. Dou, *ACS Nano*, 2021, **15**, 6316–6325.
5 X. Zhang, H. Liu, W. Wang, J. Zhang, B. Xu, K. L. Karen, Y. Zheng, S. Liu, S. Chen, K. Wang and X. W. Sun, *Adv. Mater.*, 2017, **29**, 1606405.
6 L. Zhu, Q. Lai, W. Zhai, B. Chen and Z. L. Wang, *Mater. Today*, 2020, **37**, 56–63.
7 T. Liu, W. Shi, W. Tang, Z. Liu, B. C. Schroeder, O. Fenwick and M. J. Fuchter, *ACS Nano*, 2022, **16**, 2682–2689.
8 J. T. Lin, D. G. Chen, L. S. Yang, T. C. Lin, Y. H. Liu, Y. C. Chao, P. T. Chou and C. W. Chiu, *Angew Chem. Int. Ed. Engl.*, 2021, **60**, 21434–21440.
9 Y. Cui, J. Jiang, W. Mi and Y. Xiao, *Cell Rep. Phys. Sci.*, 2023, **4**, 101299.
10 C. Yuan, X. Li, S. Semin, Y. Feng, T. Rasing and J. Xu, *Nano Lett.*, 2018, **18**, 5411–5417.
11 B. P. Bloom, Y. Paltiel, R. Naaman and D. H. Waldeck, *Chem. Rev.*, 2024, **124**, 1950–1991.
12 E. Strelcov, Q. Dong, T. Li, J. Chae, Y. Shao, Y. Deng, A. Gruverman, J. Huang and A. Centrone, *Sci. Adv.*, 2017, **3**, e1602165.
13 Z. Xiao, Z. Song and Y. Yan, *Adv. Mater.*, 2019, **31**, 1803792.
14 K. Ray, S. P. Ananthavel, D. H. Waldeck and R. Naaman, *Science*, 1999, **283**, 814–816.
15 H. Lu, J. Wang, C. Xiao, X. Pan, X. Chen, R. Brunecky, J. J. Berry, K. Zhu, M. C. Beard and Z. V. Vardeny, *Sci. Adv.*, 2019, **5**, eaay0571.
16 H. Lu, C. Xiao, R. Song, T. Li, A. E. Maughan, A. Levin, R. Brunecky, J. J. Berry, D. B. Mitzi, V. Blum and M. C. Beard, *J. Am. Chem. Soc.*, 2020, **142**, 13030–13040.
17 Y. Lu, Q. Wang, R. Chen, L. Qiao, F. Zhou, X. Yang, D. Wang, H. Cao, W. He, F. Pan, Z. Yang and C. Song, *Adv. Funct. Mater.*, 2021, **31**, 2104605.
18 A. Abhervé, N. Mercier, A. Kumar, T. K. Das, J. Even, C. Katan and M. Kepenekian, *Adv. Mater.*, 2023, **35**, 2305784.
19 S. Chen, R. Wu and H.-H. Fu, *Nano Lett.*, 2024, **24**, 6210–6217.
20 R. Naaman, Y. Paltiel and D. H. Waldeck, *Nat. Rev. Chem.*, 2019, **3**, 250–260.
21 X.-L. Peng, R.-R. Han, Y.-Z. Tang, Y.-H. Tan, X.-W. Fan, F.-X. Wang and H. Zhang, *Chem.–Asian J.*, 2023, **18**, e202201206.
22 K. Tao, Q. Li and Q. Yan, *Adv. Opt. Mater.*, 2024, **12**, 2400018.
23 C. Chen, L. Gao, W. Gao, C. Ge, X. Du, Z. Li, Y. Yang, G. Niu and J. Tang, *Nat. Commun.*, 2019, **10**, 1927.

© 2025 The Author(s). Published by the Royal Society of Chemistry

Open Access Article. Published on 04 1403. Downloaded on 28/11/1404 10:53:11 ..
This article is licensed under a Creative Commons Attribution-NonCommercial 3.0 Unported Licence.

24 M. Li, F. Fang, X. Huang, G. Liu, Z. Lai, Z. Chen, J. Hong, Y. Chen, R.-j. Wei, G.-H. Ning, K. Leng, Y. Shi and B. Tian, *Chem. Mater.*, 2022, **34**, 2955–2962.
25 Y. Zheng, J. Xu and X.-H. Bu, *Adv. Opt. Mater.*, 2022, **10**, 2101545.
26 K. Robinson, G. V. Gibbs and P. H. Ribbe, *Science*, 1971, **172**, 567–570.
27 M. Gupta and B. R. K. Nanda, *Phys. Rev. B.*, 2022, **105**, 035129.
28 S. Liu, M. W. Heindl, N. Fehn, S. Caicedo-Davila, L. Eyre, S. M. Kronawitter, J. Zerhoch, S. Bodnar, A. Shcherbakov, A. Stadlbauer, G. Kieslich, I. D. Sharp, D. A. Egger, A. Kartouzian and F. Deschler, *J. Am. Chem. Soc.*, 2022, **144**, 14079–14089.
29 M. Zhou, J. S. Sarmiento, C. Fei, X. Zhang and H. Wang, *J. Phys. Chem. Lett.*, 2020, **11**, 1502–1507.
30 W. Liang, Y. Li, D. Xiang, Y. Han, Q. Jiang, W. Zhang and K. Wu, *Acs Energy Lett.*, 2021, **6**, 1670–1676.
31 K. Michaeli and R. Naaman, *J. Phys. Chem. C.*, 2019, **123**, 17043–17048.